Published online 24 April 2009

Nucleic Acids Research, 2009, Vol. 37, No. 12 ***3887–3896***
doi:10.1093/nar/gkp257

Both helix topology and counterion distribution contribute to the more effective charge screening in dsRNA compared with dsDNA

Suzette A. Pabit, Xiangyun Qiu, Jessica S. Lamb, Li Li, Steve P. Meisburger and Lois Pollack*

School of Applied and Engineering Physics, Cornell University, Ithaca, NY 14853, USA

Received January 27, 2009; Revised April 6, 2009; Accepted April 7, 2009

ABSTRACT

The recent discovery of the RNA interference mechanism emphasizes the biological importance of short, isolated, double-stranded (ds) RNA helices and calls for a complete understanding of the biophysical properties of dsRNA. However, most previous studies of the electrostatics of nucleic acid duplexes have focused on DNA. Here, we present a comparative investigation of electrostatic effects in RNA and DNA. Using resonant (anomalous) and non-resonant small-angle X-ray scattering, we characterized the charge screening efficiency and counterion distribution around short (25 bp) dsDNA and RNA molecules of comparable sequence. Consistent with theoretical predictions, we find counterion mediated screening to be more efficient for dsRNA than dsDNA. Furthermore, the topology of the RNA A-form helix alters the spatial distribution of counterions relative to B-form DNA. The experimental results reported here agree well with ion-size-corrected non-linear Poisson–Boltzmann calculations. We propose that differences in electrostatic properties aid in selective recognition of different types of short nucleic acid helices by target binding partners.

INTRODUCTION

Strong motivation for studies of short nucleic acid helices comes from the rapid growth of research on small interfering RNA (siRNA). In this recently discovered process, short, 20-26 bp double-stranded (ds) RNA molecules participate in the control of gene regulation, causing degradation of complementary mRNA transcripts in the cytoplasm [reviewed in (1)] and initiating epigenetic processes in the nucleus [reviewed in (2)]. To date, many studies concerning the biophysical properties of nucleic acids have focused on DNA. Which results derived for DNA can be applied to understand RNA? Despite many similarities, these molecules act differently in biological systems. The dsRNA and dsDNA from viral sources have been shown to induce both shared and separate signalling pathways in mammalian cells (3). Comparative investigations of DNA and RNA molecules are necessary to establish the differences in their biophysical properties. Of particular interest is how electrostatic interactions contribute to long-range effects that eventually lead to selective recognition of RNA and DNA helices or helical sections by target proteins and nucleic acid ligands. Knowledge of electrostatic contributions to intermolecular interactions is essential for understanding nucleic acid binding modes and in developing tools for efficient packaging and delivery of synthetic molecules for oligonucleotide-based therapeutics (4).

The high-negative charge density of nucleic acids results in the association of positively charged counterions and the exclusion of negatively charged coions (5–7). This electrostatic screening allows uncharged or partially charged target binding partners access to the nucleic acid strands. Descriptions of electrostatic effects on protein–nucleic acid and inter-nucleic acid interactions abound in literature [e.g. (5,8–11)]. The accessibility of Poisson–Boltzmann-based continuum numerical calculators of electrostatic potentials around proteins and nucleic acids (12–14) enables visualization of the potential around these molecules, emphasizing probable locations of associated ions or charged ligands. While X-ray crystallography and magnetic resonance studies can pinpoint preferential regions for ion localization around nucleic acids (15–18), relatively few experimental techniques can probe the total counterion distribution around nucleic acids in solution [e.g. (19)]. In this study, we apply a unique experimental method to compare the distribution of cations associated

*To whom correspondence should be addressed. Tel: +1 607 255 8695; Fax: +1 607 255 7658; Email: lp26@cornell.edu
Present address:
Xiangyun Qiu, National Institutes of Health, Bethesda, MD20892, USA

to short dsRNA and dsDNA helices. This information provides insight into the impact of counterions on nucleic acid interactions.

RNA and DNA helices have the same charge, $-2e$/bp, but different helical structures. The 2′-OH present in RNA hinders duplex flexibility and promotes A-helix formation whereas the more malleable and polymorphic DNA duplexes prefer the B-form (20). Compared with the B-form, the A-form helix is a slightly broader and shorter molecule with a deeper and narrower major groove and a very shallow minor groove. The A-form conformation results from a larger lateral and angular displacement of the bases from the helical axis and a shorter rise per base pair, ~2.8 Å for A-RNA and ~3.4 Å for B-DNA. Although theoretical (7,21) and computational (22) considerations predict that the increased linear charge density of the A-helix will impact the ion distribution, no measurements comparing the counterion atmosphere around A-RNA and B-DNA helices have been reported.

In very low-ionic strength solution (e.g. ~1 mM NaCl), the charge screening distance, as characterized by the Debye length, is long. At even moderate duplex concentrations (of order 1 mM), the Debye length equals or exceeds the spacing between adjacent nucleic acid helices. Under these conditions, neighboring duplexes display obvious 'electrostatic repulsion' (23). As the solution ionic strength approaches physiological [e.g. ~100 Na^+ or K^+ and ~10 mM Mg^{2+} (24)], the Debye length decreases and adjacent duplexes no longer repel. In effect, the high negative charge of the duplex is screened on length scales shorter than the distance between duplexes. Previously, we applied solution small-angle X-ray scattering (SAXS) to investigate cation-mediated interaction between short dsDNA strands (25,26). Repulsion was observed at low ionic strength. As the ionic strength increased, the DNA strands appeared as isolated non-interacting molecules. Interestingly, as the ionic strength increased >10 mM $MgCl_2$, we observed end-to-end stacking of 25 bp long helices (26,27). In this case, electrostatic interactions are well-screened and neighboring duplexes approach each other, allowing weaker interactions like base stacking to dominate. Attraction consistent with precipitation was not observed for counterions of valence <3 (25). Resonant or anomalous small-angle X-ray scattering (ASAXS) was also used to probe the counterion distribution around DNA (19,28). Here, we discuss the application of these techniques to short dsRNA helices. To facilitate a straightforward DNA and RNA comparison, we chose short nucleic acids without the 2 nucleotide 3′-end overhangs which enhance siRNA-mediated gene silencing (29,30). We assess the length scale for charge screening (e.g. the Debye length) primarily by monitoring the strength of repulsion between helices. When identically prepared solutions containing dsRNA and dsDNA are studied, we find that repulsion between RNA helices vanishes at lower ionic strength; RNA helices are fully screened on shorter distances than DNA helices. We attribute this difference to two factors: enhanced counterion association, due to the higher linear charge density of A-form helices, and changes in counterion spatial distribution. In accord with previous studies (16,22), we find that ions penetrate deep inside the major groove of the A-form helix. Since ion size affects the counterion distribution and major groove penetration, we used ion-size corrected Poisson–Boltzmann-based numerical calculations and estimated an ion radius upper bound of 4 Å for effective association of ions. Our counterion studies shed some light on how target proteins or binding ligands find short RNA molecules and ultimately distinguish dsDNA from dsRNA helices. The enhanced screening of RNA results in a smaller distance of closest approach for neutral or like charged targets, and allows other shorter range interactions to take over.

MATERIALS AND METHODS

Duplex preparation

Single-stranded 25 nucleotide RNA and DNA molecules, desalted and purified, were purchased from Dharmacon (Lafayette, CO) and IDT (Coralville, IA), respectively. The DNA sequence employed (GCATCTGGGCTATA AAAGGGCGTCG) is identical to that used in previous SAXS studies (19,25,26,28) while RNA are made from ribonucleotides of the same sequence with uracil replacing thymine. The lyophilized samples were reconstituted in annealing/duplex buffer, 10 mM TRIS, 50 mM NaCl, 1 mM EDTA at pH 8.0 for DNA and 25 mM HEPES, 50 mM NaCl at pH 7.0 for RNA and the DNA–RNA hybrid. Prior to annealing, the oligonucleotide concentrations were checked by measuring absorption at 260 nm. Equimolar amounts of complimentary nucleic acid strands are mixed together and annealed at 94°C for 2 min and gradually cooled. In all experiments, absolute calibration of concentration is essential to ensure proper comparison of RNA to DNA. Duplex concentration is verified by absorption measurements at 260 nm. The extinction coefficient of the annealed duplexes, ε_{ds}, is calculated from the extinction coefficients of the single strands, ε_{s1} and ε_{s2}, using

$$\varepsilon_{ds} = (1 - h) \times (\varepsilon_{s1} + \varepsilon_{s2}) \quad \mathbf{1}$$

with hypochromicity h determined from the oligonucleotide sequence as described in (31). The measured experimental X-ray scattering intensities are proportional to concentrations measured using absorption and validate the concentration calibration described.

The duplex strands were dialyzed extensively to varying bulk salt solutions containing 1 mM pH 7 Na-MOPS (sodium 3-N-[morpholino] propanesulfonic acid) buffer using microcon centrifugal filter units (Millipore Corporation, Billerica, MA) with a 10 000 nominal molecular weight limit. The nucleic acid solutions were brought to a final volume of 40 µl. Final nucleic acid concentrations for X-ray scattering experiments ranged from 0.02 to 1 mM. All chemicals used [NaCl, $MgCl_2$, $Rb(CH_3COO)$, $Sr(CH_3COO)_2$, EDTA and MOPS] were purchased from Sigma-Aldrich (St. Louis, MO). RNAse-free TE and HEPES buffers were purchased from Fisher Scientific (Pittburgh, PA). Care was taken such that all buffers, solutions and labware used remain RNAse-free. The same

buffer solutions were used for dialysis of both DNA and RNA samples to ensure that the samples for comparison are under the same salt conditions.

SAXS experiments

Intermolecular interactions are monitored by SAXS experiments (25) which report the total scattering intensity profile, $I(q)$, from an ensemble of molecules in solution (32):

$$I(q) = I_0(q) \times S(q). \quad \mathbf{2}$$

The momentum transfer, q equals $(4\pi/\lambda)\sin\theta$, where λ is the X-ray wavelength and 2θ is the scattering angle. The form factor, $I_0(q)$, represents scattering from a single isolated molecule, while the structure factor, $S(q)$, reports interparticle interference and accounts for short range order in the sample. For isolated non-interacting molecules in dilute solution, $S(q) = 1$.

The second virial coefficient, A_2, was used as a convenient measure of the intermolecular interaction potential (27,33). A_2 is defined (33) as

$$A_2 = \frac{N_a}{2M^2}\int_V \left\{1 - \exp\left[-\frac{u(\vec{r})}{k_B T}\right]\right\} d^3\vec{r}, \quad \mathbf{3}$$

where N_a is Avogadro's number, M is the molecular weight and $u(\vec{r})$ is the intermolecular interaction potential. At fixed temperature T, the only variable that affects the sign of A_2 is $u(\vec{r})$. In general, $A_2 > 0$ signifies repulsive interactions while $A_2 < 0$ means intermolecular attraction. A_2 is derived from a linear fit of $1/S(c, q = 0)$ versus concentration c using the equation

$$\frac{1}{S(c, q = 0)} = 1 + 2MA_2c, \quad \mathbf{4}$$

where M is the molecular weight of the DNA or RNA. The structure factor at $q = 0$, $S(c, q = 0)$, was calculated by linear extrapolation of $S(q) = I(q)/I_0(q)$ at the low q region. $I(q)$ is the experimental scattering intensity while $I_0(q)$ is the computed form factor. The experimental form factor is determined at low-nucleic acid concentrations ($c \sim 0.02$ mM) and at high concentrations of monovalent salt (200 mM NaCl). The numerically determined form factor coincides with the experiment within measurement errors. The choice of using the computed form factors in the second virial calculations was governed by signal-to-noise considerations.

As a complementary measurement technique, we use ASAXS to characterize the distribution of counterions around nucleic acids (19,28,34). Note that for a two-component system defined by the nucleic acid and its corresponding counterions, the scattering profile depends on the contributions from both the nucleic acid and its counterion cloud,

$$I_0(q) = |f_{\mathrm{DNA}}F_{\mathrm{DNA}}(q) + f_{\mathrm{IONS}}F_{\mathrm{IONS}}(q)|^2, \quad \mathbf{5}$$

where f_i is the effective X-ray scattering factor and $F_i(q)$ reflects the spatial distribution of component i. $f_{\mathrm{IONS}} = N_{\mathrm{ion}}f_{\mathrm{ion}}$, where N_{ion} refers to the number of associated or condensed ions around the nucleic acid. ASAXS exploits the energy dependence of the ion scattering factor, $f_{\mathrm{ion}}(E) = f_0 + f'(E) + if''(E)$. Here, E is the incident X-ray energy. Changes in $f'(E)$ are most pronounced as E approaches an atomic resonance energy. Subtraction of two scattering intensity profiles acquired at two different X-ray energies, one well below (E_{off}) and the other near the ion atomic resonance (E_{on}), removes energy independent terms and provides the anomalous scattering signal:

$$\begin{aligned} I_{\mathrm{anom}}(q) &= I_0(q, E_{\mathrm{off}}) - I_0(q, E_{\mathrm{on}}) \\ &\approx 2f_{\mathrm{DNA}}F_{\mathrm{DNA}}(q)N_{\mathrm{ion}}[f'_{\mathrm{ion}}(E_{\mathrm{off}}) - f'_{\mathrm{ion}}(E_{\mathrm{on}})]F_{\mathrm{IONS}}(q). \end{aligned} \quad \mathbf{6}$$

We note that $I_{\mathrm{anom}}(q)$ is not an intensity *per se* but instead is proportional to the product of the Fourier transforms of the electron density of both the nucleic acid and counterions.

The ASAXS experimental set-up, including energy calibration and data acquisition, is discussed extensively in (19). A comprehensive discussion of ASAXS as a technique is given in (35,36). All X-ray scattering experiments were performed at the Cornell High Energy Synchrotron Source C1 bend magnet station producing tunable high-intensity monochromatic X-rays. SAXS profiles were acquired at X-ray energy of 10 keV as described in (25). For the ASAXS experiment, we used Rb^+ (Sr^{2+}) ions to characterize monovalent (divalent) counterions around double-stranded nucleic acids. Nominal X-ray energies used were 15.113 and 15.213 keV for Rb^+ and 16.023 and 16.123 keV for Sr^{2+}, respectively. At the energies chosen for the study, $\Delta f''(E)$ is negligible and fluorescence contributions to the scattering signal are minimal. Experimentally determined K absorption edges for Rb and Sr were 15.230 keV and 16.140 keV, respectively. The resolution of the beamline monochromator at the specified energies is 2–3 eV. The use of 3-mm thick sample holders with Silicon Nitride windows allows background subtraction and provides good signal to noise. All scattering profiles shown are averages of 16–32 individual scattering images that are radially integrated for conversion to intensity versus angular profiles. Buffer data were taken immediately before and after the nucleic acid scattering experiments to facilitate accurate background subtraction. Data taken at different beam conditions months apart are super-imposable which shows the robustness of our measurements and sample preparation techniques. Error bars from averaging multiple SAXS intensity profiles are displayed in the Supplementary Figure S1.

Numerical calculations

Numerical solutions to the non-linear Poisson–Boltzmann (NLPB) equation were obtained using the software package Adaptive Poisson–Boltzmann Solver (APBS) (13). This approach uses the detailed atomic structure of the B-form DNA and A-form RNA helices from atomic coordinates derived from the actual nucleic acid sequence and generated using the program Nucleic Acid Builder

(NAB) (37). We found good agreement of the calculated electrostatic potentials of a NAB-generated idealized helix and a high-resolution structure from the Nucleic Acid Database (NDB) (38). The calculated numbers of associated ions from NAB and NDB helices of the same sequence match with <1% percent difference. Water was described as a dielectric medium with $\varepsilon = 78.54$. Calculations were carried out assuming different probe ion radii (2, 3, 4 and 5 Å) to investigate the ion-size effects, which have been shown to affect comparison of calculations to experimental results (28,39). The scattering form factor $I_0(q)$ was calculated from the nucleic acid atomic coordinates and APBS-based distribution of counterions and dummy hydration shell atoms [described in (25)]. The calculated form factors match form factors experimentally determined using conditions where there is no inter-nucleic acid interactions ($c \sim 0.02$ mM). Anomalous scattering signals were generated from the difference of calculated form factors at two different X-ray energies defined by the ASAXS experiment. $\Delta f'(E)$, the energy-dependent change in the scattering form factor used in the calculations, $-7.3\,e$ for Rb and $-6.5\,e$ for Sr, were taken from atomic scattering factor data (40). APBS course mesh dimensions used were $120 \times 120 \times 200$ Å^3 and fine mesh dimensions were $90 \times 90 \times 165$ Å^3. The number of grid points in the x-, y-, and z-directions were $161 \times 161 \times 161$. For these sufficiently large calculation boxes, calculations are only weakly dependent on grid size with <2% change in the computational results when box dimensions are changed by as much as 30%. The NLPB equation was solved using the 'Multiple Debye-Hückel' boundary condition. To obtain the number of counterions and map the ion density as a function of distance from the cylindrical axis of dsDNA or dsRNA, we integrated the number density of each type of ion over the whole box employed in the APBS computation. The box is defined by a set potential: $-0.5\,k_BT/e$ for counting 'bound' ions and $1.5\,k_BT/e$ for anomalous signal and ion density calculations. Various thermodynamic criteria have been used in the literature to determine the number of associated ions (41,42). The value $-0.5\,k_BT/e$ is chosen so that the number of 'bound' monovalent cations neutralize 76% of the DNA charge, as expected from the Manning condensation theory (7) [validated by (43–45) and references within]. In the middle section of the molecule, the distance from the center of the helical axis defined by $-0.5\,k_BT/e$ varies slightly with the choice of probe ion radius, with nominal values of 25.8 Å for DNA and 24.7 Å for RNA when a 3 Å probe ion radius is used.

RESULTS

RNA charge screening is more efficient than DNA

Here, we compare ionic strength dependent interactions of 25 bp DNA and RNA at duplex concentrations ranging from 0.1 to 1 mM. Nucleic acid samples were prepared by dialysis against solutions containing 0, 3, 6, 16 and 133 mM $MgCl_2$ in pH 7, 1 mM Na-MOPS buffer (see Methods section). Divalent cations were employed instead of monovalent cations because of their stronger influence on inter-nucleic acid potentials (25).

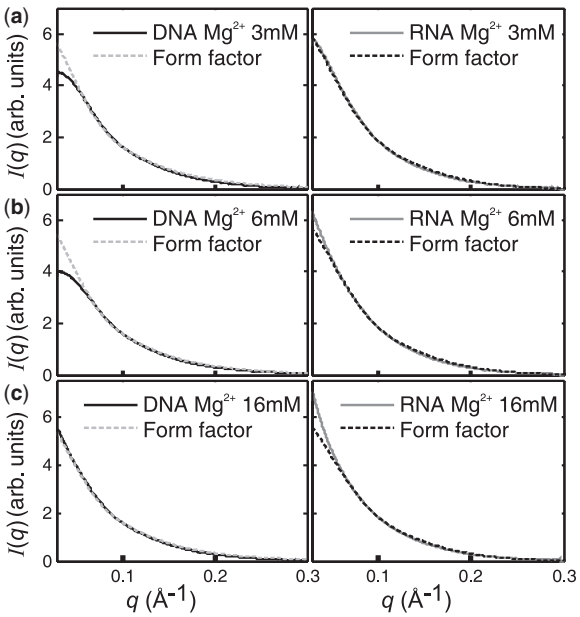

Figure 1. DNA and RNA SAXS profiles $I(q)$ compared with form factors $I_0(q)$. Curves that fall below the form factor indicate repulsive behavior while those above the form factor denote attraction. Nucleic acid solutions are (**a**) in bulk salt concentration of 3 mM $MgCl_2$, with matching DNA and RNA concentrations of 0.6 mM; (**b**) in 6 mM $MgCl_2$, [DNA] = [RNA] = 1.1 mM; and (**c**) in 16 mM $MgCl_2$, [DNA] = [RNA] = 0.6 mM. Note the data in (**b**) were acquired at higher nucleic acid concentration than that of (**a**) and (**c**) to emphasize differences between DNA and RNA. SAXS curves were normalized to each other at $0.08 < q < 0.13$ Å^{-1} to allow direct comparison of scattering profiles. In this regime, under all conditions probed, the SAXS profiles are identical to the computed form factor, $I_0(q)$, the scattering profile of a non-interacting molecule. The computed form factors match, within error, the experimental form factors measured at very low nucleic acid concentrations, where interparticle interference effects are negligible.

SAXS enables direct comparison of inter-nucleic acid interactions in RNA and DNA as a function of ionic strength of the solution. X-ray scattering profiles shown in Figure 1 were acquired on DNA and RNA samples with nominally matched duplex concentrations. To assess interparticle interactions, each DNA and RNA SAXS intensity profile, $I(q) = I_0(q) \times S(q)$, is compared with the form factor $I_0(q)$ (dashed line), which represents the scattering profile of non-interacting duplexes. The effect of interstrand interactions is most strongly reflected by changes in $S(q)$ at the lowest values of q ($q < 0.05$ Å^{-1}). Curves that fall below the form factor $I_0(q)$ indicate inter-DNA repulsion while those with y-intercepts above the form factor denote attraction, in this case end-to-end stacking.

At 3 mM Mg^{2+}, the scattering from DNA strands falls below the form factor at the lowest q, indicating repulsion. Conversely, the RNA scattering profile coincides with the form factor; the RNA strands do not interact. Since the duplex concentration is the same for both experiments, RNA exhibits enhanced screening relative to

DNA (Figure 1a). At 6 mM Mg^{2+} (Figure 1b), the low q portion of the DNA scattering profile again falls below the form factor, indicating repulsion. In contrast, the low q portion of the RNA scattering profile lies above the form factor indicating weak attraction. The shape of these curves is consistent with end-to-end stacking, previously reported in DNA (26,27). At 16 mM Mg^{2+}, the DNA scattering profile rises above the form factor, indicating weak attraction, while the RNA scattering profile displays more prominent attraction (Figure 1c). At the highest [Mg^{2+}] studied, 133 mM, attraction is measured for both DNA and RNA. Supplementary Figure S1 illustrates SAXS profiles denoting repulsion, no interaction and attraction. Supplementary Figure S2 shows scattering from a 25 bp DNA–RNA hybrid which forms the A-helix (20). The scattering profile of the hybrid was measured at 6 mM Mg^{2+}, where the DNA and RNA scattering profiles showed clear differences. The hybrid more closely resembles RNA than DNA.

To quantify the intermolecular interaction potentials, we computed the second virial coeffients A_2 [described in Methods Section and (27)] under a variety of salt conditions (see Figure 2 and the expanded figure in Supplementary Figure S3). $A_2 > 0$ implies repulsion between like-charged helices while $A_2 < 0$ implies a predominantly negative intermolecular potential leading to attraction (27,33). For 25 bp DNA duplexes, the shift from repulsion to attraction occurs when the free Mg^{2+} concentration equals 10 mM Mg^{2+}, as in (25,26). In contrast, the shift from repulsion to attraction occurs just above 3 mM Mg^{2+} for RNA, illustrating that RNA is more efficiently screened than DNA. This point derives additional support from the onset of end-to-end stacking which occurs at lower [Mg^{2+}] in RNA than in DNA. Since the duplexes must approach each other before they stack, electrostatic repulsion must be more rapidly diminished in RNA than in DNA (even at the ends where it is already reduced). As is true for DNA, the RNA scattering profiles are well fit by a linear combination of 25 and 50 bp calculated form factors (Supplementary Figure S4). End-to-end stacking of DNAs has been reported in experiments by different groups (27,46). Recently, end-to-end stacking of short RNAs has also been observed, albeit at high concentration (47). The range of end effects on the electrostatic potential and thermodynamic properties have been explored computationally for DNA (48,49), and recent experimental data show that end-to-end stacking free energies of DNA and RNA are nearly equal (46,47). Thus, end effects are not expected to play a role in the difference between RNA and DNA. In summary, the changeover from repulsion to attraction in RNA occurs at lower Mg^{2+} concentrations compared to DNA, indicating more efficient screening. Although it has long been anticipated that a higher linear charge density attracts more counterions (7), previous experimental demonstration of this effect was derived by extrapolation from observations that electrophoretic mobility of dsDNA is faster than dsRNA of the same total charge (50,51). Here, we validate the predictions by direct measurement.

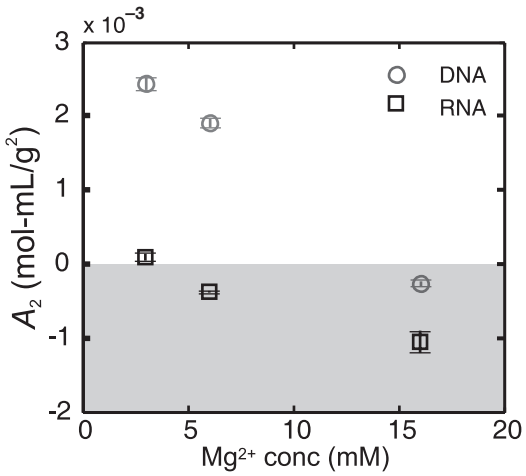

Figure 2. DNA and RNA second virial coefficients A_2 as a function of [Mg^{2+}]. A_2 provides a measure of the strength of intermolecular interactions. Repulsion is lost and the onset of attraction occurs at lower bulk ion concentrations in RNA than in DNA. The attractive regime ($A_2 < 0$) is shaded gray to aid the eye.

Ions are distributed closer to RNA than to DNA

Experimental results shown in Figure 2 clearly indicate differences in counterion interactions with DNA or RNA. However, these results do not address differences in the spatial distribution of the ions. To address this point, we employed ASAXS to probe the distribution of monovalent and divalent counterions around RNA and DNA molecules. For these studies, RNA and DNA at duplex concentrations of 0.2 mM were prepared in pH 7, 1 mM Na-MOPS buffer and 100 mM $Rb(CH_3COO)$ or 100 mM $Sr(CH_3COO)_2$ salt solutions. ASAXS curves are generated by subtracting on-edge SAXS profiles from off-edge SAXS profiles as described in (19). Rb^+ (Sr^{2+}) ions were used instead of Na^+ (Mg^{2+}) due to X-ray energy accessibility.

To effectively compare counterion distributions, it is important to assess the impact of the different underlying structures of A-RNA and B-DNA on scattering profiles. Figure 3a shows predicted scattering profiles from RNA and DNA helices with no added counterions [from the software package CRYSOL (52)]. Plotting the intensity on a logarithmic scale highlights differences between these profiles as q increases. Note that $I(0)$ is proportional to the square of the sample molecular weight (53). Thus, the difference between the profiles at the lowest q is not surprising since the molecular weight of 25 bp dsRNA is 1.04× >25 bp dsDNA. The most interesting feature in this comparison is the predicted crossing of the two curves at $q \approx 0.17$ Å^{-1}. X-ray scattering from a larger object generally falls off more rapidly with angle (or q) than the scattering from a smaller object (54). Since nucleic acids are roughly cylindrical, the scattering profiles are governed by two length scales. Contributions from the larger length scales (nucleic acid lengths) dominate at the lower q region of the data while the higher q region ($q > 0.17$ Å^{-1}) emphasizes contributions from the shorter length scales (helix diameters). The crossover and rapid

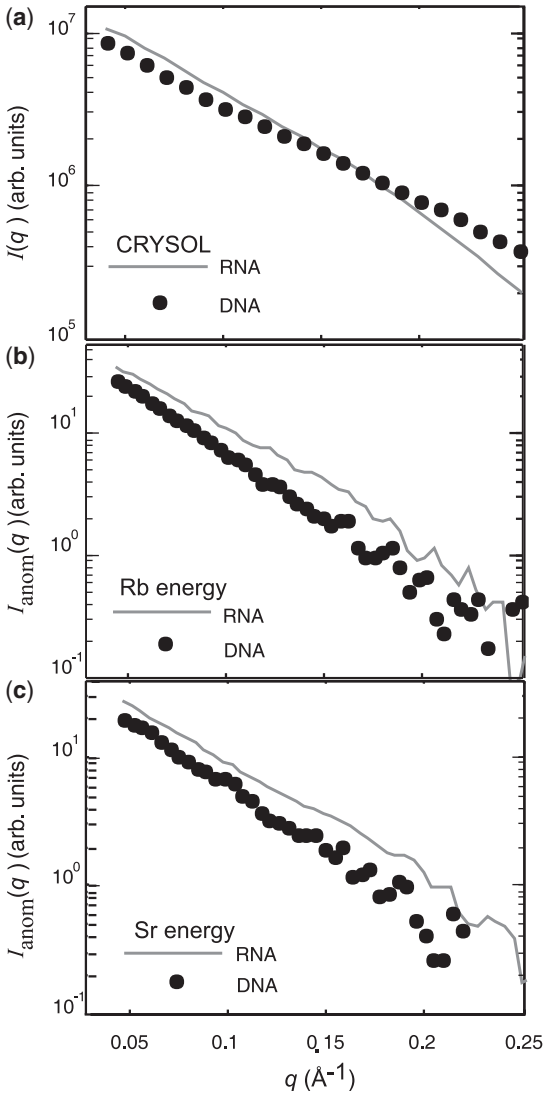

Figure 3. Distibution of ions around DNA and RNA. CRYSOL-predicted scattering profiles (**a**) in the absence of ions. Experimental ASAXS profiles for nucleic acids in (**b**) 100 mM Rb^+, and (**c**) 100 mM Sr^{2+}; [DNA] = [RNA] = 0.2 mM. ASAXS curves were normalized using factors from the extrapolated scattering intensity at $q = 0$, $I(0)$, weighted by the square of the sample molecular weight. $I(0)$ were determined by Guinier analysis of the low energy (E_{off}) SAXS curves (53).

decay in RNA scattering at high q in the CRYSOL profiles (Figure 3a) follow from the geometry of the A-RNA, which is larger in diameter than B-DNA.

The experimental ASAXS profiles, $I_{anom}(q)$, contain contributions from both the ion and nucleic acid electron densities. If the ion distribution around RNA and DNA closely followed the underlying nucleic acid, we would expect the ASAXS curves to mirror the shape of the CRYSOL predicted scattering profile; the RNA signal should decay faster than the DNA signal at mid to high q. Figure 3b and c show the ASAXS signals from DNA and RNA in monovalent and divalent counterion atmospheres. The ASAXS curves do not cross, and furthermore, the anomalous scattering from the RNA at higher q is more pronounced than the signal from DNA. In ASAXS, the shape of the anomalous signal reflects the set of all vectors that have one end inside the nucleic acid and the other in the ion cloud. Since anomalous signals persisting to higher q signify a set of shorter vectors linking nucleic acid and ions, this measurement suggests that counterions are more closely localized to the RNA than the DNA. Thus, the DNA-ion cross section is larger than the RNA-ion cross section. This trend is observed for both monovalent (Rb, Figure 3b) and divalent (Sr, Figure 3c) signals, indicating that monovalent and divalent counterions associate more closely to RNA than DNA.

Numerical calculation of ion distribution

We modeled the ion–nucleic acid association by numerical calculation of anomalous signals using the NLPB formalism. NLPB adequately predicts the distribution of monovalent ions around nucleic acids (34,55). As in previous studies (19,28,39), application of NLPB to ion condensation problems required consideration of ion sizes in the calculations, a convenient feature of the APBS (13). Ion radii of 2, 3, 4 and 5 Å were tested. The results of the calculations depend significantly on the choice of probe ion radius r, as this parameter limits the distance of closest approach of the ion to the nucleic acid. The calculated ASAXS curves best reflect the experimental results when $r = 4$ Å. Figure 4 shows the amplitude-normalized experimental ASAXS curves for a bulk solution of 100 mM monovalent ions plotted with the theoretical ASAXS curves for ion radius of 3, 4 and 5 Å. Below $r = 5$ Å, the calculated DNA ASAXS curves decay more rapidly than the RNA ASAXS profiles. At larger radii (e.g. $r = 5$ Å), this trend reverses and the anomalous signals calculated for RNA decay more rapidly than for DNA. Since this reversal does not manifest in the experimental curves, an ion radius upper bound of 4 Å is necessary to describe ion association with the RNA surface. This choice of ion radius upper bound is further validated by the corresponding radial Patterson inversions (56) shown in Figure 5. The calculated anomalous signals of DNA and RNA in 100 mM divalent ions show behavior similar to the monovalent ions (Supplementary Figures S5 and S6). Similar conclusions can be drawn from application of NLPB models to divalent ions; however, deviations from the continuum theory are more pronounced for divalent as opposed to monovalent ions (55,57).

DISCUSSION

RNA appears charge neutral at lower bulk Mg^{2+} concentrations

By comparing measured SAXS profiles with computed form factors, and calculating second virial coefficients, A_2, we have determined when the duplexes repel, attract or do not interact. All of our results are consistent with a picture in which RNA's charge is more efficiently screened than DNA's. Repulsion vanishes at lower free ion concentrations, allowing other, presumably shorter range

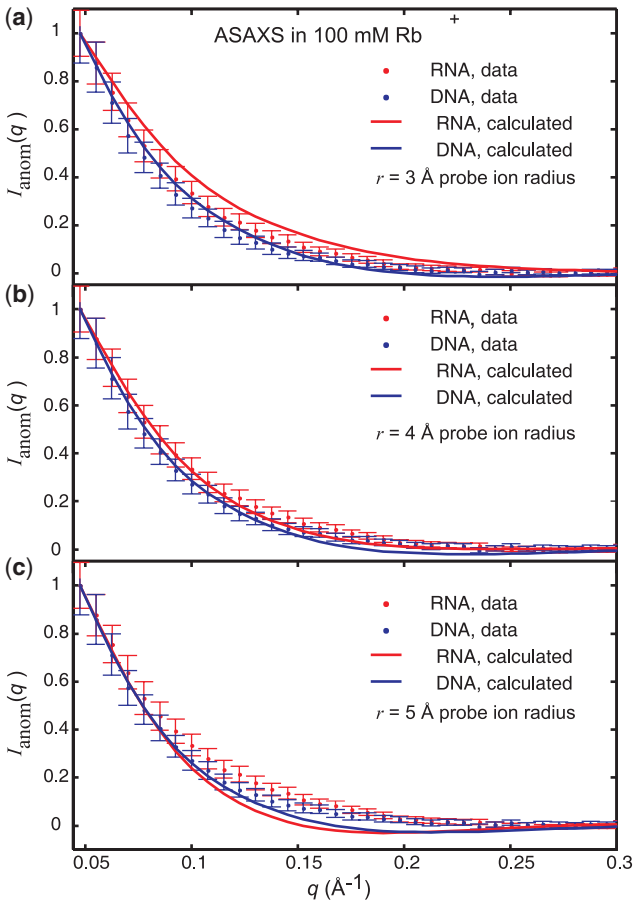

Figure 4. Comparison of experimental and calculated ASAXS profiles of DNA and RNA shown in 100 mM monovalent ions. Calculated anomalous signals using varying probe ion radius (**a**) 3; (**b**) 4; and (c) 5 Å, are shown. All curves were normalized by matching at the lowest q to facilitate comparison of experiment to theory.

interactions to take over at lower bulk ionic strength. At 3 mM Mg^{2+}, RNA strands do not interact ($A_2 \approx 0$), while DNA strands repel ($A_2 > 0$). At 6 mM Mg^{2+} and above, attraction consistent with end-to-end stacking of RNAs is measured, while a similar effect in DNA does not occur until the $[Mg^{2+}] \geq 16$ mM. Note that DNA–RNA hybrid duplexes behave more like dsRNA than dsDNA (Supplementary Figure S2). Since DNA–RNA hybrids are A-form helices, helix topology must play a central role in charge screening efficiency.

A $-0.5\,k_BT/e$ potential shell

We can calculate the total number of 'bound' ions from the numerical NLPB solution by integrating the number density of each type of ion over a finite box employed in the computation, expressed by a potential cutoff of $-0.5\,k_BT/e$. Here, 'bound' ions refer to those localized near the nucleic acid surface ['diffuse' ions in (6)], but not specifically site-bound. For a probe ion radius of 4 Å, we find that the average numbers of 'bound' monovalent counterions around the RNA and DNA are 37.2 and 35.9, respectively (also see Supplementary Figure S7). Therefore, using the same potential surface, more 'bound' counterions are found around RNA than DNA.

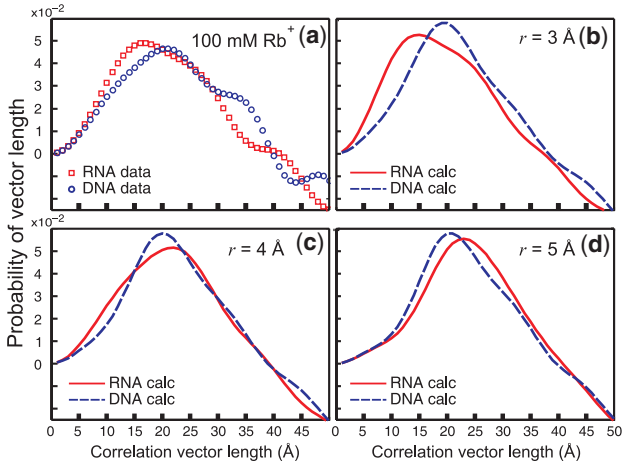

Figure 5. Radial Patterson inversion of the anomalous difference signal calculated using $U(R) = R\int sI_{anom}(s)\sin(2\pi sR)ds$ as described by Engelman *et al.* (56), $s = q/2\pi$. Ideally, $U(R)$ reports the lengths of vectors correlating nucleic acids with condensed counterions. (**a**) $U(R)$ of 100 mM Rb^+ ASAXS data. In addition, $U(R)$ computed from the APBS simulations for varying probe ion radius of (**b**) 3; (**c**) 4; and (**d**) 5 Å are shown. From this representation, it is clear that an ion radius upper bound of 4 Å is necessary to describe the data.

Note that a difference of 1–2 ions may be below the resolution of ion counting experiments like equilibrium dialysis (55), comparative fluorescence (58) and absorbance (59) measurements. Defining the same negative surface potential around DNA and RNA accounts for the geometrical differences between the helices and allows a quantitative comparison of ions localized near the nucleic acid surface. Previous calculations of associated ion quantity on A- and B-DNA helices by Mills *et al.* (12) utilized a large radial boundary of 24 Å. Though claiming that the same number of ions surrounds A- and B-form helices, they found significant counterion density in the A-form major groove compared with the B-form. Instead of a uniform distance, we assert that defining an isoenergy surface is a better method for comparing the number of associated ions.

As suggested by the ASAXS results (Figure 3), ions are more closely localized to the RNA central axis than DNA, likely via A-form major groove penetration. Figure 6 shows the monovalent ion density as a function of distance from the cylindrical axis of DNA and RNA as predicted by NLPB. (Ion density calculations for divalent ions are shown in Supplementary Figure S8.) Two peaks are associated with RNA: the first is due to ions inside the deep major groove while the second represents ions in the outer opening of the groove. These two binding modes are postulated from the X-ray crystal structures by Robinson *et al.* (16) and suggested by Chin *et al.* (12). Our data support the viewpoint that positive counterions are attracted to negative potential wells in the deep major groove of A-RNA and the minor groove of B-DNA thereby minimizing like-charge repulsion, and facilitating or stabilizing molecular interactions (12,16,17,22).

What is the allowable ion size that can penetrate the A-form major groove? The A-form major groove width

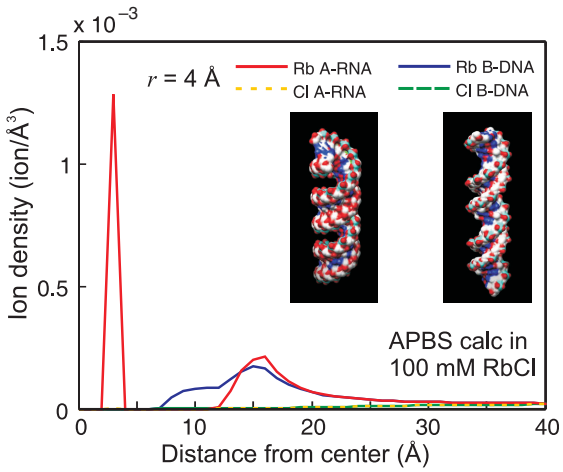

Figure 6. NLPB-generated ion density as function of distance from the cylindrical axis of DNA and RNA for 100 mM RbCl, probe ion radius of 4 Å. Ions can come closer to the RNA surface through the deeper major groove. Inset shows a comparison of the major groove sizes, DNA and RNA helices are tilted equally to display the grooves. The PDB structures were generated using NAB (37) and drawn using Chimera (60).

is reported to be small, $\sim 3-6$ Å (20,61). The size of hexahydrate Mg^{2+} ions found inside the A-form major groove in the crystal structure is ~8 Å (16), however, the authors postulate that facile exchange of coordinated water molecules is necessary to allow hydrated Mg^{2+} ions to enter the groove without hindrance. We used the ion radius feature of APBS to constrain the possibilities, e.g. to determine whether or not an ion can enter the groove. The ion radius in APBS computations simply signifies the probe radius rolled over the van der Waals surface of the molecule. A probe ion radius of 5 Å leads to results that are in disagreement with our ASAXS data (Figures 4 and 5; Supplementary Figures S5 and S6) and displays no ions in the RNA major groove region (Supplemenatry Figure S8). Thus, our experimental results suggest that there is an upper bound of physically relevant ion radius of 4 Å. Note that APBS is a continuum model with its own limitations. Though it allows for modifications of probe ion radius and ion valence, it does not make a distinction based on other ion properties like valence- and hydration-shell sizes and Hofmeister series effects (62). Nonetheless, it is a powerful first-order approximation since it considers the atomic coordinates and hence, provides a useful assessment of molecular topology.

Biophysical and biological implications

Simple electrostatic arguments cannot fully explain the difference between dsRNA and dsDNA. The higher linear charge density of A-RNA results in associated counterions that are closer to each other and to the RNA surface than in DNA. In the simplest planar approximation of Rouzina and Bloomfield (21), dsRNA yields a higher number of surface ions compared to dsDNA. While basic physics predicts more associated counterions (50), computation of the electrostatic potential distribution emphasizes potential wells for ion localization, such as the deep major groove of A-form RNA (12). Thus, the difference between dsRNA and dsDNA cannot be attributed to linear charge density alone; molecular structure plays an important role. The distinction between RNA and DNA is important in understanding counterion-driven processes like DNA condensation and RNA folding. Moreover, proper caution must be employed when using models based on DNA to understand RNA interactions and RNA folding.

In the crowded cellular environment where molecular motions are largely governed by random processes like diffusion, how individual molecules locate their correct binding partners remains an open question. Differences in charge screening efficiency between DNA and RNA helices may bias this search. RNA helices are more efficiently screened and in the right ion environment can appear charge neutral at distances farther away from the helical axis than DNA. Since this makes the distance of closest approach shorter in RNA, charge neutral protein domains are able to move closer to the RNA surface. This facilitates sequence-specific and short range interactions [e.g. reviewed in (63–65)] to take over. In our experiment, we have shown that as the charge of short dsRNA helices are screened by Mg^{2+} ions, nonelectrostatic end-to-end stacking interactions become favorable. Although we have not observed inter-RNA stacking *in vivo*, this result can be used to elucidate siRNA interactions. Tryptophans of an siRNA binding protein have been shown to bracket terminal base pairs of the siRNA duplex (66) and salt concentration has been shown to affect the siRNA binding activity of this RNA silencing suppressor protein (10). Further studies of electrostatic contributions to siRNA recognition must include the effect of the 2 nucleotide 3′-end overhangs and the 5′-end phosphorylation which seem to be important in siRNA-mediated gene silencing (29,30).

Interest in siRNAs as potent therapeutic agents is growing (4). One challenge facing siRNA-based therapeutics is the effective intracellular delivery of active molecules. Recent work showed that using packaging and delivery parameters optimized for DNA does not necessary lead to efficient siRNA gene silencing (67). Distribution of small synthetic dsRNA may be affected by stacking interactions and counterion association. End-to-end stacked oligonucleotides exceed the optimal activation lengths (<30 bp) and can initiate an anti-viral defensive response *in vivo* (68). Therefore, finding optimal counterion conditions could be essential in packaging synthetic siRNA bundles for successful intracellular delivery.

CONCLUSIONS

SAXS measurements show that ion mediated screening is more efficient in dsRNA compared with dsDNA. ASAXS results suggest that the more effective screening seen in RNA occurs because A-RNA draws monovalent and divalent ions closer. The experimental results agree well with NLPB-based calculations of anomalous signals for a probe ion radius of 4 Å. For the same NLPB-defined potential surface close to the nucleic acids, we find more

'bound' ions close to RNA than DNA. We also show that ions are able to come closer to the central axis of the RNA duplex through a deeper major groove. This distinction is important in understanding selective recognition of different types of short nucleic acid helices by target binding partners.

SUPPLEMENTARY DATA

Supplementary Data are available at NAR Online.

ACKNOWLEDGEMENTS

We thank Ken Finkelstein for experimental assistance at Cornell High Energy Synrchrotron Source, Kurt Andresen for useful discussions, Hye Yoon Park for help with data acquisition and Phil Bevilacqua for advice on handling of RNA samples.

FUNDING

National Science Foundation (grant MCB-0347220); Cornell Nanobiotechnology Center; National Institutes of Health (grants P01-GM066275 and T32-GM008267); is National Science Foundation (to Cornell High Energy Synchrotron Source (CHESS); National Institutes of Health (to Cornell High Energy Synchrotron Source (CHESS); (to National Institute of General Medical Sciences (grant DMR-9713424 to National Institutes of Health (grant P41RR-01081); Molecular graphics images were produced using the UCSF Chimera package from the Resource for Biocomputing, Visualization, and Informatics at the University of California, San Francisco).

Conflict of interest statement. None declared.

REFERENCES

1. Filipowicz,W., Jaskiewicz,L., Kolb,F. and Pillai,R. (2005) Post-transcriptional gene silencing by siRNAs and miRNAs. *Curr. Opin. Struct. Biol.*, **15**, 331–341.
2. Matzke,M. and Birchler,J. (2005) RNAi-mediated pathways in the nucleus. *Nat. Rev. Genet.*, **6**, 24–35.
3. Cheng,G., Zhong,J., Chung,J. and Chisari,F. (2007) Double-stranded DNA and double-stranded RNA induce a common antiviral signaling pathway in human cells. *Proc. Natl Acad. Sci. USA*, **104**, 9035–9040.
4. Juliano,R., Alam,M., Dixit,V. and Kang,H. (2008) Mechanisms and strategies for effective delivery of antisense and siRNA oligonucleotides. *Nucleic Acids Res.*, **36**, 4158–4171.
5. Sharp,K. and Honig,B. (1995) Salt effects on nucleic acids. *Curr. Opin. Struct. Biol.*, **5**, 323–328.
6. Draper,D. (2004) A guide to ions and RNA structure. *RNA*, **10**, 335–343.
7. Manning,G. (1969) Limiting laws and counterion condensation in polyelectrolyte solutions. I. Colligative properties. *J. Chem. Phys.*, **51**, 924–933.
8. Draper,D., Grilley,D. and Soto,A. (2005) Ions and RNA folding. *Annu. Rev. Biophys. Biomol. Struct.*, **34**, 221–243.
9. Law,M., Linde,M., Chambers,E., Oubridge,C., Katsamba,P., Nilsson,L., Haworth,I. and Laird-Offringa,I. (2006) The role of positively charged amino acids and electrostatic interactions in the complex of U1A protein and U1 hairpin II RNA. *Nucleic Acids Res.*, **34**, 275–285.
10. Koukiekolo,R., Sagan,S. and Pezacki,J. (2007) Effects of pH and salt concentration on the siRNA binding activity of the RNA silencing suppressor protein p19. *FEBS Lett.*, **581**, 3051–3056.
11. Lemaire,P., Anderson,E., Lary,J. and Cole,J. (2008) Mechanism of PKR activation by dsRNA. *J. Mol. Biol.*, **381**, 351–360.
12. Chin,K., Sharp,K., Honig,B. and Pyle,A. (1999) Calculating the electrostatic properties of RNA provides new insights into molecular interactions and function. *Nature Struct. Biol.*, **6**, 1055–1061.
13. Baker,N., Sept,D., Joseph,S., Holst,M. and McCammon,J. (2001) Electrostatics of nanosystems: Application to microtubules and the ribosome. *Proc. Natl Acad. Sci. USA*, **98**, 10037–10041.
14. Grochowski,P. and Trylska,J. (2008) Review: continuum molecular electrostatics, salt effects, and counterion binding – a review of the Poisson-Boltzmann theory and its modifications. *Biopolymers*, **89**, 93–113.
15. Robinson,H. and Wang,A. (1996) Neomycin, spermine and hexaamminecobalt(III) share common structural motifs in converting B- to A-DNA. *Nucleic Acids Res.*, **24**, 676–682.
16. Robinson,H., Gao,Y., Sanishvili,R., Joachimiak,A. and Wang,A. (2000) Hexahydrated magnesium ions bind in the deep major groove and at the outer mouth of A-form nucleic acid duplexes. *Nucleic Acids Res.*, **28**, 1760–1766.
17. Tereshko,V., Minasov,G. and Egli,M. (1999) A 'hydrat-ion' spine in a B-DNA minor groove. *J. Am. Chem. Soc.*, **121**, 6970–6970.
18. Shui,X., McFail-Isom,L., Hu,G. and Williams,L. (1998) The B-DNA dodecamer at high resolution reveals a spine of water on sodium. *Biochemistry*, **37**, 8341–8355.
19. Andresen,K., Qiu,X., Pabit,S., Lamb,J., Park,H., Kwok,L. and Pollack,L. (2008) Mono- and trivalent ions around DNA: A small-angle scattering study of competition and interactions. *Biophys. J.*, **95**, 287–295.
20. Saenger,W. (1984) *Principles of Nucleic Acid Structure*. Springer-Verlag, New York, pp. 220–266.
21. Rouzina,I. and Bloomfield,V. (1997) Competitive electrostatic binding of charged ligands to polyelectrolytes: Practical approach using the non-linear Poisson-Boltzmann equation. *Biophys. Chem.*, **64**, 139–155.
22. Mills,P., Rashid,A. and James,T. (1992) Monte-carlo calculations of ion distributions surrounding the oligonucleotide d(ATATATATA T)$_2$ in the B, A, and wrinkled D conformations. *Biopolymers*, **32**, 1491–1501.
23. Koch,M., Sayers,Z., Sicre,P. and Svergun,D. (1995) A synchrotron radiation electric field x-ray solution scattering study of DNA at very low ionic strength. *Macromolecules*, **28**, 4904–4907.
24. Alberts,B., Johnson,A., Lewis,J., Raff,M., Roberts,K. and Walter,P. (2002) *Molecular Biology of the Cell*, 4th edn. Garland Science, New York, p. 616.
25. Qiu,X., Kwok,L., Park,H., Lamb,J., Andresen,K. and Pollack,L. (2006) Measuring inter-DNA potentials in solution. *Phys. Rev. Lett.*, **96**, 138101.
26. Qiu,X., Andresen,K., Kwok,L., Lamb,J., Park,H. and Pollack,L. (2007) Inter-DNA attraction mediated by divalent counterions. *Phys. Rev. Lett.*, **99**, 038104.
27. Li,L., Pabit,S., Lamb,J., Park,H. and Pollack,L. (2008) Closing the lid on DNA end-to-end stacking interactions. *Appl. Phys. Lett.*, **92**, 223901.
28. Andresen,K., Das,R., Park,H., Smith,H., Kwok,L., Lamb,J., Kirkland,E., Herschlag,D., Finkelstein,K. and Pollack,L. (2004) Spatial distribution of competing ions around DNA in solution. *Phys. Rev. Lett.*, **93**, 248103.
29. Elbashir,S., Martinez,J., Patkaniowska,A., Lendeckel,W. and Tuschl,T. (2001) Functional anatomy of siRNAs for mediating efficient RNAi in *Drosophila melanogaster* embryo lysate. *EMBO J.*, **20**, 6877–6888.
30. Bolcato-Bellemin,A., Bonnet,M., Creusatt,G., Erbacher,P. and Behr,J. (2007) Sticky overhangs enhance siRNA-mediated gene silencing. *Proc. Natl Acad. Sci. USA*, **104**, 16050–16055.
31. Tataurov,A., You,Y. and Owczarzy,R. (2008) Predicting ultraviolet spectrum of single stranded and double stranded deoxyribonucleic acids. *Biophys. Chem.*, **133**, 66–70.
32. Svergun,D. and Koch,M. (2003) Small-angle scattering studies of biological macromolecules in solution. *Rep. Prog. Phys.*, **66**, 1735–1782.

33. Bonnete,F. and Vivares,D. (2002) Interest of the normalized second virial coefficient and interaction potentials for crystallizing large macromolecules. *Acta. Crystallogr.*, **D58**, 1571–1575.
34. Das,R., Mills,T., Kwok,L., Maskel,G., Millett,I., Doniach,S., Finkelstein,K., Herschlag,D. and Pollack,L. (2003) Counterion distribution around DNA probed by solution x-ray scattering. *Phys. Rev. Lett.*, **90**, 188103.
35. Ballauff,M. and Jusufi,A. (2006) Anomalous small-angle x-ray scattering: analyzing correlations and fluctuations in polyelectrolytes. *Colloid Polym. Sci.*, **284**, 1303–1311.
36. Horkay,F., Hecht,A., Rochas,C., Basser,P. and Geissler.,E. (2006) Anomalous small angle x-ray scattering determination of ion distribution around a polyelectrolyte biopolymer in salt solution. *J. Chem. Phys.*, **125**, 234904.
37. Macke,T. and Case,D. (1998) In Leontes,N. and SantaLucia,J.J. (eds), *Molecular Modeling of Nucleic Acids*, American Chemical Society, Washington DC, pp. 379–393.
38. Berman,H., Olson,W., Beveridge,D., Westbrook,J., Gelbin,A., Demeny,T., Hsieh,S.-H., Srinivasan,A. and Schneider,B. (1992) The nucleic acid database: a comprehensive relational database of three-dimensional structures of nucleic acids. *Biophys. J.*, **63**, 751–759.
39. Chu,V., Bai,Y., Lipfert,J., Herschlag,D. and Doniach,S. (2007) Evaluation of ion binding to DNA duplexes using a size-modified Poisson–Boltzmann theory. *Biophys. J.*, **93**, 3202–3209.
40. Henke,B., Gullikson,E. and Davis,J. (1993) X-ray interactions: photoabsorption, scattering, transmission, and reflection at $E = 50$–30000 eV, $Z = 1$–92. *Atomic Data and Nuclear Data Tables*, **54**, 181–342.
41. Diehl,A. and Levin,Y. (2004) Effective charge of colloidal particles. *J. Chem. Phys.*, **121**, 12100–12103.
42. Mukherjee,A., Schmitz,K. and Bhuiyan,L. (2002) Comparison of the thermal and concentration criteria for determining the effective charge of a spherical colloidal particle in a salt-free suspension. *Langmuir*, **18**, 4210–4219.
43. Record,M. Jr, Lohman,T. and De Haseth,P. (1976) Ion effects on ligand-nucleic acid interactions. *J. Mol. Biol.*, **107**, 145–158.
44. Manning,G. (1979) Counterion binding in polyelectrolyte theory. *Acc. Chem. Res.*, **12**, 443–449.
45. Anderson,C. and Record,M. Jr. (1982) Polyelectrolyte theories and their applications to DNA. *Ann. Rev. Phys. Chem.*, **33**, 191–222.
46. Nakata,M., Zanchetta,G., Chapman,B., Jones,C., Cross,J., Pindak,R., Bellini,T. and Clark,N. (2007) End-to-end stacking and liquid crystal condensation of 6-to 20-base pair DNA duplexes. *Science*, **318**, 1276–1279.
47. Zanchetta,G., Bellini,T., Nakata,M. and Clark,N. (2008) Physical polymerization and liquid crystallization of RNA oligomers. *J. Am. Chem. Soc.*, **130**, 12864–12865.
48. Allison,S. (1994) End effects in electrostatic potentials of cylinders: models for DNA fragments. *J. Phys. Chem.*, **98**, 12091–12096.
49. Olmsted,M., Anderson,C. and Record,M. Jr. (1989) Monte carlo description of oligoelectrolyte properties of DNA oligomers: range of end effect and the approach of molecular and thermodynamic properties to the polyelectrolyte limits. *Proc. Natl Acad. Sci. USA*, **86**, 7766–7770.
50. Gast,F. and Hagerman,P. (1991) Electrophoretic and hydrodynamic properties of duplex ribonucleicacid molecules transcribed *in vitro*: evidence that A-tracts do not generate curvature in RNA. *Biochemistry*, **30**, 4268–4277.
51. Bonifacio,G., Brown,T., Conn,G. and Lane,A. (1997) Comparison of the electrophoretic and hydrodynamic properties of DNA and RNA oligonucleotide duplexes. *Biophys. J.*, **73**, 1532–1538.
52. Svergun,D., Barberato,C. and Koch,M. (1995) CRYSOL – a program to evaluate x-ray solution scattering of biological macromolecules from atomic coordinates. *J. Appl. Crystallogr.*, **28**, 768–773.
53. Cantor,C. and Schimmel,P. (1980) *Biophysical Chemistry Part II: Techniques for the Study of Biological Structure and Function*, W.H. Freedman and Company, New York, 811–819.
54. Glatter,O. and Kratky,O. (1982) *Small Angle X-ray Scattering*. Academic Press, New York, pp. 3–13.
55. Bai,Y., Greenfeld,M., Travers,K., Chu,V., Lipfert,J., Doniach,S. and Herschlag,D. (2007) Quantitative and comprehensive decomposition of the ion atmosphere around nucleic acids. *J. Am. Chem. Soc.*, **129**, 14981–14988.
56. Engelman,D., Moore,P. and Schoenborn,B. (1975) Neutron scattering measurements of separation and shape of proteins in 30s ribosomal subunit of *Escherichia coli*: S2–S5, S5–S8, S3–S7. *Proc. Natl Acad. Sci. USA*, **72**, 3888–3892.
57. Tan,Z. and Chen,S. (2007) RNA helix stability in mixed Na^+/Mg^{2+} solution. *Biophys. J.*, **92**, 3615–3632.
58. Grilley,D., Soto,A. and Draper,D. (2006) Mg2+-RNA interaction free energies and their relationship to the folding of RNA tertiary structures. *Proc. Natl Acad. Sci. USA*, **103**, 14003–14008.
59. Krakauer,H. (1971) The binding of Mg^{++} ions to polyadenylate, polyuridylate, and their complexes. *Biopolymers*, **10**, 2459–2490.
60. Pettersen,E., Goddard,T., Huang,C., Couch,G., Greenblatt,D., Meng,E. and Ferrin,T. (2004) UCSF Chimera – A visualization system for exploratory research and analysis. *J. Comput. Chem.*, **25**, 1605–1612.
61. Xiong,Y. and Sundaralingam,M. (1998) Crystal structure and conformation of a DNA-RNA hybrid duplex with a polypurine RNA strand: d(TTCTTBr^{5}CTTC)-r(GAAGAAGAA). *Structure*, **6**, 1493–1501.
62. Baldwin,R. (1996) How Hofmeister ion interactions affect protein stability. *Biophys. J.*, **71**, 2056–2063.
63. Pabo,C. and Sauer,R. (1984) Protein-DNA recognition. *Ann. Rev. Biochem.*, **53**, 293–321.
64. Chen,Y. and Varani,G. (2005) Protein families and RNA recognition. *FEBS J.*, **272**, 2088–2097.
65. Chang,K. and Ramos,A. (2005) The double-stranded RNA-binding motif, a versatile macromolecular docking platform. *FEBS J.*, **272**, 2109–2117.
66. Ye,K., Malinina,L. and Patel,D. (2003) Recognition of small interfering RNA by a viral suppressor of RNA silencing. *Nature*, **426**, 874–878.
67. Bouxsein,N., McAllister,C., Ewert,K., Samuel,C. and Safinya,C. (2007) Structure and gene silencing activities of monovalent and pentavalent cationic lipid vectors complexed with siRNA. *Biochemistry*, **46**, 4785–4792.
68. Akhtar,S. and Benter,I. (2007) Nonviral delivery of synthetic siRNAs *in vivo*. *J. Clin. Invest.*, **117**, 3623–3632.